Title: A high-resolution, cloud-assimilating numerical weather prediction model for solar irradiance forecasting.

Authors: Patrick Mathiesen[1], Craig Collier[2], and Jan Kleissl[1] (corresponding author)

[1]Department of Mechanical and Aerospace Engineering, University of California, San Diego.
9500 Gilman Dr., La Jolla, CA, 92093-0411, USA.
Phone: +1 858 534 8087, email: jkleissl@ucsd.edu

[2]GL-Garrad Hassan
9665 Chesapeake Drive #435, San Diego, CA, 92123, USA.

Abstract:
It is well established that most operational numerical weather prediction (NWP) models consistently over-predict irradiance. While more accurate than imagery-based or statistical techniques, their applicability for day-ahead solar forecasting is limited. Overall, error is dependent on the expected meteorological conditions. For regions with dynamic cloud systems, forecast accuracy is low. Specifically, the North American Model (NAM) predicts insufficient cloud cover along the California coast, especially during summer months. Since this region represents significant potential for distributed photovoltaic generation, accurate solar forecasts are critical.

To improve forecast accuracy, a high-resolution, direct-cloud-assimilating NWP based on the Weather and Research Forecasting model (WRF-CLDDA) was developed and implemented at the University of California, San Diego (UCSD). Using satellite imagery, clouds were directly assimilated in the initial conditions. Furthermore, model resolution and parameters were chosen specifically to facilitate the formation and persistence of the low-altitude clouds common to the California coast. Compared to the UCSD pyranometer network, intra-day WRF-CLDDA forecasts were 17.4% less biased than the NAM and relative mean absolute error (rMAE) was 4.1% lower. For day-ahead forecasts, WRF-CLDDA accuracy did not diminish; relative mean bias error was only 1.6% and rMAE 18.2% (5.5% smaller than the NAM). Spatially, the largest improvements occurred for the morning hours along coastal regions when cloud cover is expected. Additionally, the ability of WRF-CLDDA to resolve intra-hour variability was assessed. Though the horizontal (1.3 km) and temporal (5 min.) resolutions were fine, ramp rates for time scales of less than 30 min. were not accurately characterized. Thus, it was concluded that the cloud sizes resolved by WRF-CLDDA were approximately five times as large as its horizontal discretization.

Keywords: Solar forecasting; High-resolution numerical weather prediction (NWP); Direct cloud assimilation

1. Introduction

The accurate characterization of cloud fields, their evolution, and their optical properties is critical for solar irradiance forecasting. For short-term forecasting, imagery based cloud-advection techniques (Perez *et al.*, 2010 and Chow *et al.*, 2011) provide excellent characterizations of cloud fields and cloud motion. However, clouds are highly dynamic and cloud properties can change drastically over just a few hours. As such, the accuracy of frozen-cloud advection techniques diminishes significantly over the first six hours. For forecast horizons exceeding 5 hours (on average), physics-based weather models (numerical weather prediction (NWP)) are generally regarded as the most accurate method for predicting solar irradiance (Fig. 2 of Perez *et al.*, 2010).

Though more accurate than cloud-motion techniques for long forecast horizons, previous studies have conclusively demonstrated consistent and systematic errors in NWP irradiance forecasts. Remund *et al.* (2008) compared several months of irradiance forecasts from three NWP sources: The National Digital Forecast Database (NDFD), the European Centre for Medium-range Weather Forecasts (ECMWF), and the Weather and Research Forecasting (WRF) model as initialized by the Global Forecasting System (GFS). Generally, mean bias errors (MBE) for day-ahead hourly forecasts were positive indicating a consistent under-prediction of cloud cover and/or cloud optical depth. For the three models, hourly root-mean square errors (RMSE) ranged from 87 W m^{-2} to 223 W m^{-2}. Perez *et al.* (2010) validated hourly irradiance forecasts derived from the NDFD against seven ground measurement stations across the continental US. Over one year, RMSE was at least 150 W m^{-2} and increased for forecast horizons of greater than one day. Similarly, Lorenz *et al.* (2009) validated intra-day ECWMF irradiance forecasts for more than 200 ground measurement locations in Germany over a year. Excluding night-time hours, relative RMSE (RMSE normalized by the average daily irradiance) was near 40%. Furthermore, irradiance was consistently over-predicted, particularly for moderately cloudy conditions near mid-day (MBE ≈ 100 W m^{-2}). Lorenz *et al.* (2009) attributed this to incorrect modeled cloud water content and deficient cloud optical thickness. Mathiesen and Kleissl (2011) found comparable systematic errors when comparing the North American Mesoscale (NAM), GFS, and ECMWF models' irradiance forecasts to ground measurements in the US over about a year. For all models, MBE exceeded 30 W m^{-2} and RMSE was larger than 110 W m^{-2}. Again, a general under-prediction of cloud cover was observed. Out of all measured cloudy conditions, 52.4% were forecast incorrectly as clear by the NAM. Additionally, Mathiesen *et al.* (2012) related NAM forecast accuracy to location and the likelihood of cloud cover for hourly data in California. Due to the high probability of cloud cover, summertime coastal forecasts were strongly biased (MBE > 125 W m^{-2}). Inland, where cloudy conditions were less likely, NAM forecasts were less biased. Pelland *et al.* (2011) observed similar trends in Environment Canada's Global Environmental Multiscale (GEM) model. Relative MBE (MBE normalized by the average observed irradiance) for hourly data ranged from 0% to 14% and relative RMSE exceeded 16.7%. Lastly, Lara-Fanego *et al.* (2011) compared hourly intra-day irradiance forecasts from a 3-km WRF model driven by the GFS to four ground measurement sites in southern Spain. Here, MBE ranged from 49 to 64 W m^{-2} and RMSE was 136-170 W m^{-2}. Regardless of model, irradiance NWP forecasts are generally biased high. This consistent under-prediction of cloud cover demonstrates the limitations of the current operational NWP for solar irradiance forecasting.

Coarse model resolutions and inadequate physics parameterizations contribute to NWP cloud cover error. The operational NWP models generally have spatial resolutions on the order of 10 km or larger. In this configuration, it is impossible to resolve fine-scale cloud features or even large convective clouds. Tselioudis and Jakob (2002) compared ECMWF T42 ($\Delta x \approx 2.5°$) and T106 ($\Delta x \approx 1°$) cloud forecasts to

satellite observations and found that the higher-resolution T106 model generally predicted cloud coverage and cloud properties more accurately for all meteorological regimes. Similarly, Lin *et al.* (2009) compared cloud forecasts of multiple nested WRF simulations that ranged in resolution from 20 to 0.8 km. While large scale features were qualitatively captured by all models, simulations with spatial resolutions coarser than 4 km tended to under-predict cloud cover. Additionally, the parameterization of physical processes, specifically the simulation of cloud microphysics and planetary boundary layer (PBL) mixing, has a large impact on cloud and irradiance forecast accuracy. Otkin and Greenwald (2008) thoroughly catalogued the effect that different physics parameterizations have on WRF simulated cloud fields.

Additionally, accurate model initialization is critical for NWP forecast accuracy. Often, initial conditions derived from large-scale models contain the error of the parent model. To minimize inherited error, observation data can be assimilated into the initial conditions. Data assimilation is the specification of model initial conditions using the optimal combination of coarse-scale model output and observations. Typically, temperature, pressure, and velocity initializations are modified to match observation. However, since most operational data-assimilation techniques omit cloud observations, benefits of data assimilation for cloud-cover and irradiance forecasting are unknown. Notably, the Rapid Update Cycle (RUC, Benjamin *et al.*, 2004a) uses a cloud-analysis system to assimilate cloud observations into the model initial conditions. In this system, satellite imagery, radar data, and local cloud cover reports are used to construct a three-dimensional observed cloud field matrix. Clouds are built into the initial conditions by directly modifying the model hydrometeors (cloud and water mixing ratios) and the state variables which support them (Benjamin *et al.* 2002, 2004b, Weygandt *et al.*, 2006, and Hu *et al.*, 2007). Similar systems (Albers *et al.*, 1996) are in use in the Center for Analysis and Prediction of Storms' (CAPS) Advanced Regional Prediction System (ARPS, Xue *et al.*, 2003).

In this study, a new, high-resolution, cloud-assimilating NWP model is developed and tested at the University of California, San Diego (UCSD) for solar irradiance forecasting (WRF-CLDDA). Using fine spatial resolution, physics parameterizations that promote cloud-cover formation, and a cloud-assimilation system, this model is specifically designed to minimize the errors typically associated with NWP irradiance forecasts (Section 2, Section 4). Using WRF-CLDDA, irradiance forecasts are produced for the summer period (5/1/11 – 6/30/11) and validated against a dense UCSD pyranometer network. During this time, marine layer stratocumulus clouds (Section 5.1) are common. Optically thick, these clouds often reduce irradiance by as much as 75%. Additionally, since their evaporation is spatially correlated, large positive irradiance ramps can occur simultaneously over extensive regions. Since marine layer clouds are co-located with regions that have high-potential for distributed generation solar photovoltaic generation (the southern California coast), their accurate prediction is critical. WRF-CLDDA hourly-average irradiance forecasts are calculated and compared to NAM forecasts and ground observations (Section 5.2). Finally, the ability of WRF-CLDDA to resolve detailed, high-resolution cloud fields is tested by comparing forecast irradiance variability, expressed as a ramp-rate distribution, to observed variability (Section 5.3). Overall, it is shown that clouds are successfully populated into the initial conditions and that WRF-CLDDA irradiance forecasts are significantly more accurate than the NAM, especially during marine layer cloud conditions.

2. Numerical Weather Prediction (NWP) Models

2.1 The North American Mesoscale Model (NAM)

One of several operational NWP models for the continental United States, the North American Mesoscale Model (NAM) is based on the WRF-Non-Hydrostatic Mesoscale Model (WRF-NMM) and is

maintained by the National Centers for Environmental Prediction (NCEP). The NAM uses 12 km horizontal resolution and 60 vertical hybrid sigma-level terrain-following coordinates. Temporally, the time step size is 30s and output is available hourly to a maximum forecast horizon of 36 hours. The NAM model is initialized by the NAM Data Assimilation System at 00, 06, 12, and 18 UTC daily using observations and GFS data. Data is assimilated using the three-dimension variational (3DVAR) grid-point statistical interpolation (GSI) method (Rogers *et al.*, 2009). Assimilated data include temperature, pressure, relative humidity, and wind magnitudes/directions as determined from radiosonde, satellite, and other observations (Wu *et al.*, 2002). Initialized shortly before the North American sunrise, irradiance forecasts from the 12 UTC run are slightly more accurate and were exclusively used in this study. Full details of the NAM are available in Janjic *et al.*, 2010 and Janjic *et al.*, 2011.

Within the NAM, cloud evolution is primarily dependent on the Ferrier cloud microphysics package (Rogers *et al.*, 2001). Here, two prognostic water variables are used: water vapor and a total condensate variable. Cloud water, cloud ice, and other water variables are diagnostically split from the condensate variable. Additionally, vertical transport has a large impact on cloud formation. To account for sub-grid scale convection and resolve vertical transport, the Betts-Miller-Janjic (Janjic, 1994, and Janjic, 2000) cumulus parameterization is used. Finally, irradiance at the surface is calculated using the Geophysical Fluid Dynamics Laboratory Short Wave (GFDL-SW, Lacis and Hansen, 1974) radiative transfer model (RTM). In addition to cloud cover, the background absorption from carbon dioxide and ozone is accounted for. Since the GFDL-SW RTM is called only once per hour, the impact of intra-hour cloud cover variability on irradiance is unresolved. Lastly, since the GFDL-SW is a columnar RTM adjacent grid cells have no influence on surface irradiance.

Two other NWP models are commonly used for forecasting in North America but were omitted in this study: The Global Forecasting System (GFS) and the Rapid Refresh (RAP). Though the GFS was previously shown to be less biased than the NAM for solar forecasting (Mathiesen and Kleissl, 2011), its coarse horizontal resolution (0.5°) limits its ability to resolve differences in cloud cover over short distances which is critical for coastal California solar forecasting. Additionally, despite a sophisticated initialization scheme, the RAP was excluded due to its short maximum forecast horizon (18 hours) and lack of full intra-day and day-ahead forecasts.

2.2 The Weather and Research Forecasting Model (WRF)

The Weather and Research Forecasting (WRF, Skamarock *et al.*, 2008) model is a highly customizable numerical weather prediction model that is maintained by the National Center for Atmospheric Research (NCAR). In this study, WRF V3.4 is configured with three-nests of horizontal resolutions of 12 km, 4 km, and 1.3 km (Fig. 1, centered at the University of California, San Diego). Boundary conditions for the outer domain are derived from the NAM. To facilitate low-altitude marine layer stratocumulus formation, the domain is vertically divided into 75 terrain-following levels, 50 of which are below 3000 m. The model time-step size is defined dynamically according to a Courant-Freidrichs-Lewy (CFL) criterion of 0.3. This ensures that the distance of horizontal advection occurring in a single time step does not exceed the discretization size. Downward short-wave irradiance fields are output every 5 min to a maximum forecast horizon of 36 hours.

Cloud microphysics is parameterized using the Thompson microphysics package (Thompson *et al.*, 2004). Previously, Otkin and Greenwald (2008) demonstrated that the Thompson scheme produced accurate WRF-simulated cloud fields while maintaining efficient computation time. The Thompson model is a hybrid single/double moment parameterization that explicitly predicts the interaction

between six classes of water (water vapor, cloud water, rain, cloud ice, snow, and graupel) in addition to the cloud ice number concentration. To support marine layer stratocumulus formation, the cloud condensation nuclei (CCN) concentration for water clouds is fixed at 300 cm^{-3} (Hudson and Frisbie, 1991). Furthermore, planetary boundary layer (PBL) mixing is parameterized using the Mellor-Yamada-Nakanishi-Niino scheme (MYNN, Nakanishi and Niino, 2006). Like in the NAM, sub-grid scale vertical mixing is unresolved in the coarse (Δx = 12 km) domain and the Kain-Fritsch (Kain, 2004) cumulus parameterization is applied. For the inner nests ($\Delta x \leq 4$ km) it is assumed that all vertical motion is explicitly resolved and no cumulus parameterization is used. Finally, irradiance is calculated using the MM5 short-wave scheme (Dudhia, 1989) which takes into account cloud reflection, cloud absorption, water vapor absorption, and clear-sky scattering.

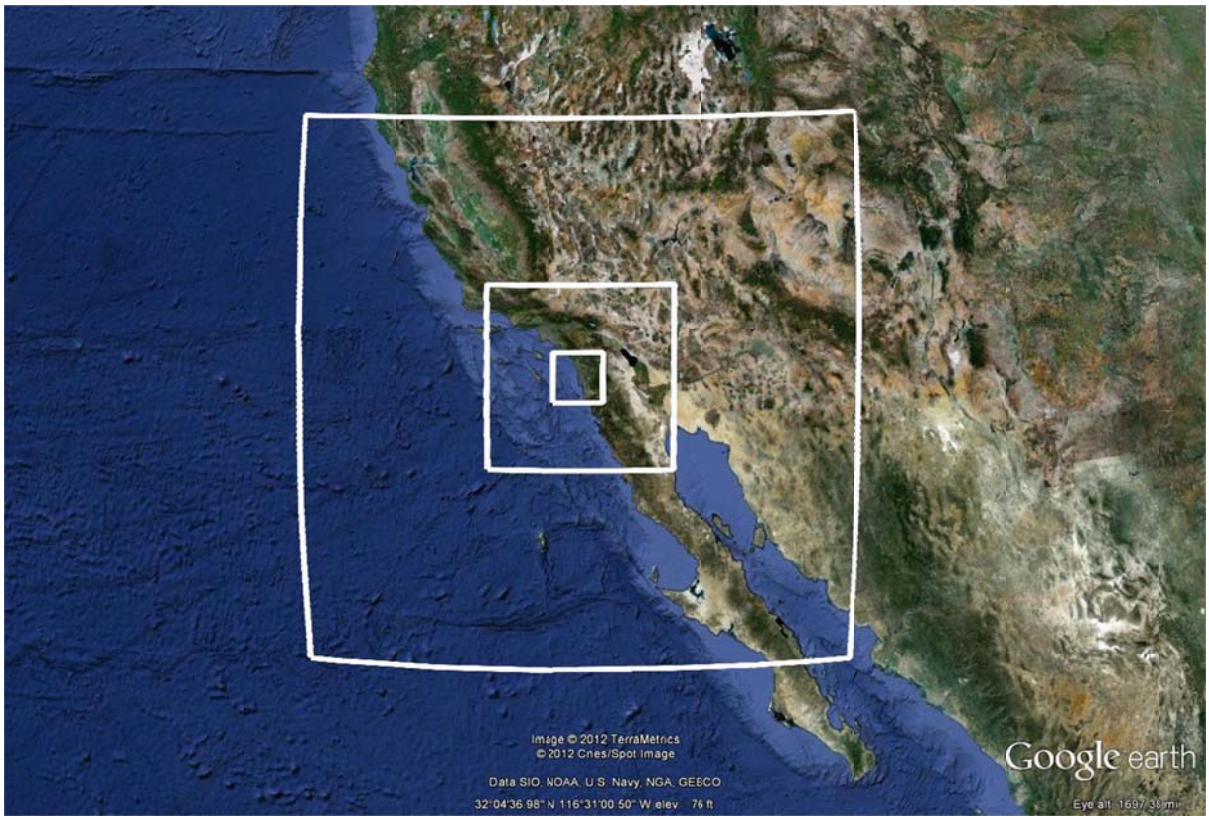

Figure 1: WRF-CLDDA nest configuration (Δx = 12 km, 4 km, 1.3 km) centered at the University of California, San Diego using Google Earth.

3. Assimilation and Validation Data Sources

3.1 GOES Cloud and SolarAnywhere Irradiance Data

Cloud field information is determined using Geostationary Operational Environmental Satellite (GOES) imagery. GOES Solar Insolation Project (GSIP) level-2 data provides cloud-top-temperature (CTT) with 4 km x 4 km spatial resolution (Sengupta *et al.*, 2010). To remove noise, CTT data is spatially convolved to 12 km horizontal resolution. Furthermore, clouds spanning less than 3 adjacent pixels (< 12 km) are filtered from the data and data that is missing or outside of historical limits is ignored.

Additionally, SolarAnywhere (SolarAnywhere, 2012) provides irradiance data on a 0.01° (≈ 0.94 km in southern California) resolution grid. Irradiance data is derived by calculating a cloud index from GOES imagery (Perez *et al.*, 2002). The cloud index in conjunction with a clear sky model is used to calculate irradiance. Previously, Perez *et al.* (2010) has shown that SolarAnywhere data to have RMSE between 77 W m^{-2} and 112 W m^{-2} when compared to the nationwide Surface Radiation (SURFRAD) network.

3.2 DEMROES Irradiance Network

Decision Making using Real-time Observations for Environmental Sustainability (DEMROES) is a high-density network of weather stations located at the University of California, San Diego. In addition to meteorological data such as wind speed/direction, temperature, and precipitation, global horizontal solar irradiance at the surface (GHI) is measured at 1 Hz to within ±5% (Campbell Scientific, 1996) using Licor LI-200SZ photodiode pyranometers. To match WRF-CLDDA/NAM GHI output, 1 s irradiance data is temporally averaged to 5 min or 1 hr. Furthermore, to ensure that similar spatial scales are being compared between NWP and observed data, DEMROES GHI measurements are averaged across WRF-simulated grid cells prior to comparison. In this study, only the cell containing six DEMROES stations was analyzed (Fig. 2, red dots).

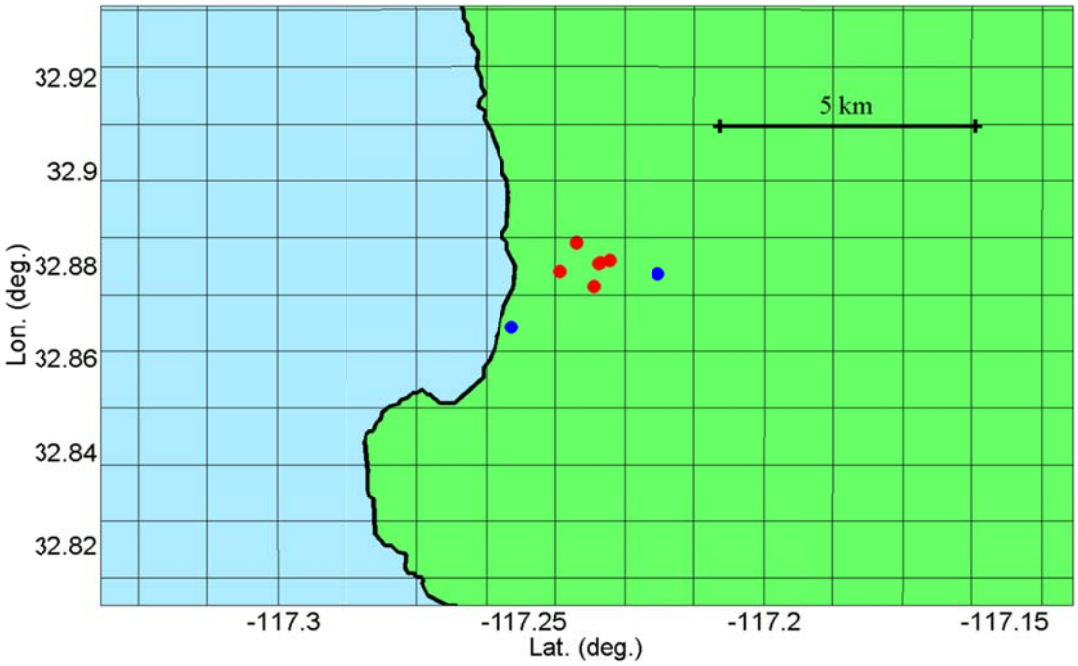

Figure 2: Map of WRF-CLDDA grid cells (Δx = 1.3 km) and DEMROES pyranometer locations (red circles). Blue circles show DEMROES sites that were not analyzed and the black line demarks the Pacific coast.

4. Methodology

4.1 WRF Cloud Assimilation System (WRF-CLDDA)

In standard data assimilation, observations are used to produce an optimal estimate for the initial conditions of the state variables (e.g. pressure, temperature, relative humidity, etc.). The cloud microphysics model in conjunction with the modified state variables is subsequently relied upon to accurately populate the initial conditions with clouds. As cloud hydrometeors are not directly initialized into the model, several hours of simulation time (known as 'spin-up') are required to develop the initial cloud field. Since the benefit of data assimilation often disappears over the first few hours

(Novakovskaia *et al.*, 2011), this 'indirect' approach becomes impractical as clouds formed from assimilated data are nearly always outdated. Alternatively, direct cloud assimilation initializes clouds nearly instantaneously by raising water vapor mixing ratios to supersaturation, forcing the microphysics scheme to convert excess water vapor to clouds.

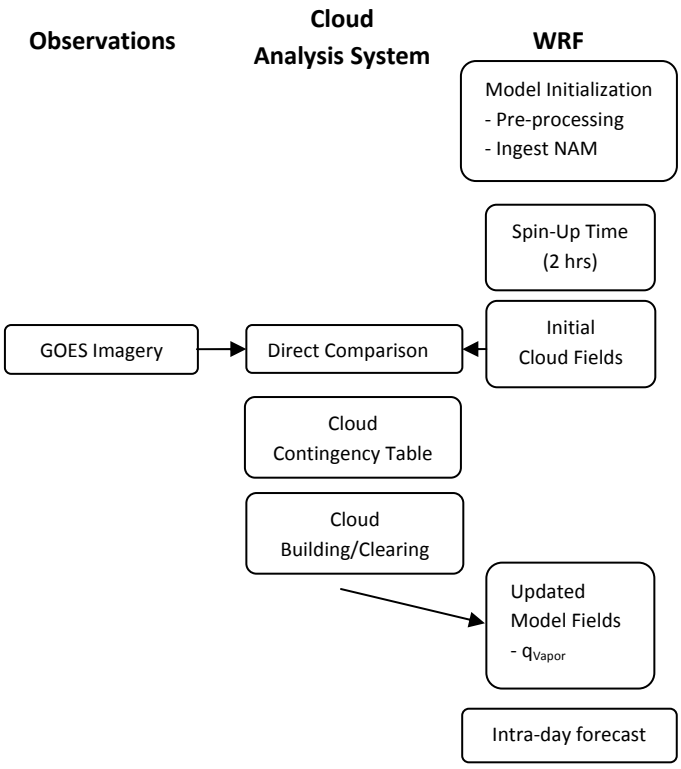

Figure 3: WRF-CLDDA direct cloud assimilation system overview.

Figure 3 depicts a general outline of the WRF-CLDDA forecast system. The direct-cloud assimilation is based on Benjamin *et al.* (2002, 2004b), Albers *et al.* (1996) and Hu *et al.* (2007). First, the WRF model is initialized with 12 UTC NAM data. For two simulation hours, WRF is spun-up with redundant 12 UTC NAM boundary conditions. In this way, NAM provided initial conditions such as wind velocity and pressure are downscaled to match the high-resolution WRF-domain topography. To initialize cloud cover, GOES satellite imagery is first co-located onto the WRF grid. Horizontally, the convolved CTT field is matched to WRF coordinates via nearest neighbor interpolation. In coastal California, the dominant overnight cloud structure consists of stable marine stratocumulus clouds (Sec. 5.1). Assuming this cloud structure, model cloud-top location is fixed to the base of the columnar temperature inversion. In general, cloud thickness increases with inversion height (Appendix A). As such, model cloud base is calculated according to

$$z_{c,base} = 0.45 \cdot H_{Inv.};\ H_{Inv.} < 750\ m \quad \text{(Eq. 1)}$$

$$z_{c,base} = 0.28 \cdot H_{Inv.} + 127.5;\ H_{Inv.} \geq 750\ m \quad \text{(Eq. 2)}$$

where $z_{c,base}$ is the base of the cloud and $H_{inv.}$ is the altitude of the temperature inversion. If no temperature inversion is predicted within the column, cloud-top pressure is instead calculated via the intersection of the WRF-simulated vertical temperature profile and observed CTT. Finally, the 2-D cloud-

top and cloud-base location maps are combined to produce a 3-D binary matrix of cloud location co-located with the WRF domain. This cloud contingency table determines the action for cloud-building and -clearing in the domain initial conditions.

Assimilated cloud water content is determined via WRF-simulated temperature and pressure profiles. The saturation water vapor mixing ratio (w_s) is defined by

$$w_s = \varepsilon \frac{e_s}{P - e_s} \quad \text{(Eq. 3)}$$

where P is pressure, e_s is the saturation water vapor pressure, and ε is the ratio of the gas constants of moist and dry air. e_s, however, depends on temperature and is defined by the Clausius-Clapeyron Equation (Eq. 4 in hPa):

$$e_s = 6.11 \exp\left(-\frac{L_v}{R_v}\left(\frac{1}{277.16} - \frac{1}{T} \right) \right) . \quad \text{(Eq. 4)}$$

Here, L_v is the latent heat of vaporization, R_v is the gas constant for moist air, and T is air temperature (in K). For observed cloudy cells, w_s is calculated using the WRF-simulated temperature and q_{vapor} is raised to 110% of saturation using Eq. 5:

$$q_{vapor} = 1.1 w_s \ . \quad \text{(Eq. 5)}$$

Raising q_{vapor} to 110% of saturation generally produces clouds that are optically similar to the marine stratocumulus clouds observed in coastal California. Excess water in supersaturated grid cells is immediately converted from q_{vapor} to cloud water (q_{cloud}) or cloud ice (q_{ice}) via the microphysics simulation of cloud condensation. During this process, latent heat is released causing an unintended increase in model air temperature. To avoid this side-effect, microphysics heating in WRF is disabled for the hour following cloud assimilation. For grid cells without GOES cloud cover, q_{vapor} is reduced to a maximum of 75% of saturation. Figure 4 shows an example of the cloud assimilation result for June13, 2011. For areas observed as cloudy (green in 4a), columnar q_{vapor} (4b) is large. Over the eastern Gulf of California, higher temperatures result in larger saturation water vapor mixing ratios (w_s) and subsequently higher concentrations of q_{vapor} (Eq. 5).

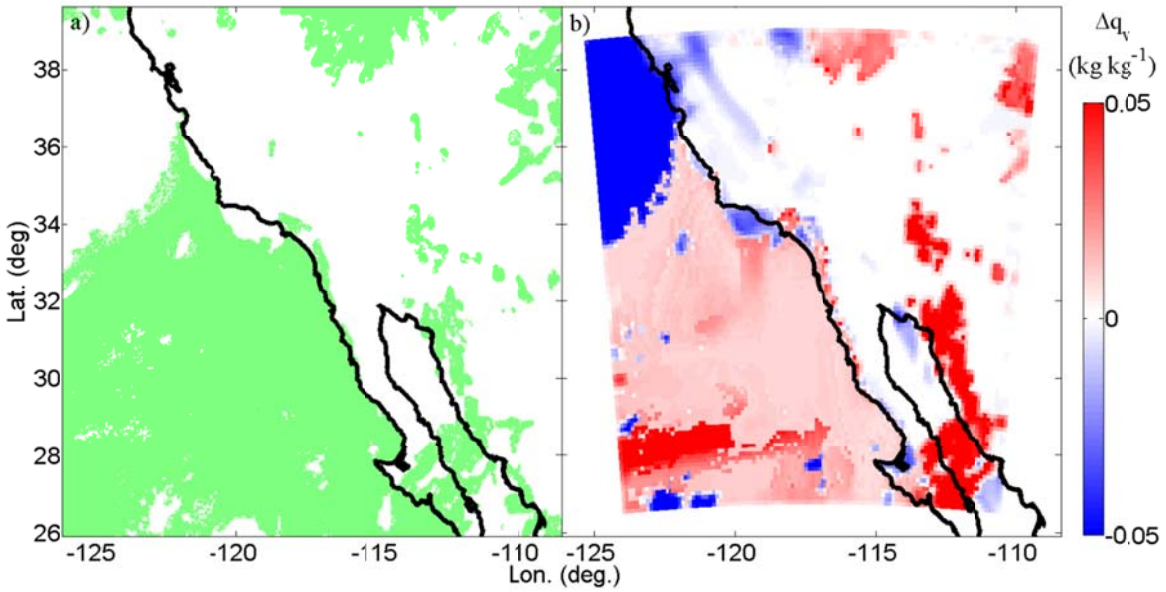

Figure 4: a) GOES cloud mask, where green is cloudy and white is clear and b) Δq_{vapor} (kg kg^{-1}) for assimilated initial conditions on 6/13/2011.

Several further steps are performed to ensure numerical stability. To avoid disagreement with the specified boundary conditions, data assimilation is not performed for the outer 5 points on each side of the domain. Furthermore, numerical instability manifested as unphysical, rapid waves can be triggered by large gradients. To avoid creating artificial water vapor gradients through data assimilation, the q_{vapor} field is smoothed horizontally via convolution for all cells within 30 km of cloud-building cells. Vertically, spline interpolation is used to smooth q_{vapor} within 7 levels.

4.2 Validation and Error Metrics

WRF-CLDDA irradiance forecasts were created for summer months when marine stratocumulus clouds are common in coastal California (5/1/11 – 6/30/11). Forecasts were initialized at 12 UTC and simulated to a maximum forecast horizon of 36 hours. For three days (6/19/11, 6/20/11, and 6/21/11) GSIP cloud data was unavailable and results from these initializations were omitted in the analysis. Validation was separated into three distinct categories: Cloud cover comparison, irradiance error metrics, and variability analysis.

First, a qualitative analysis of a WRF-CLDDA forecast was performed. The formation and dissipation of marine layer clouds common to the study period was discussed. For each hour, the columnar cloud mixing ratio (q_{cloud}) and GHI from WRF-CLDDA were examined and related to the typical pattern of marine layer cloud cover. Furthermore, a WRF-CLDDA GHI time-series was qualitatively compared to observation.

Secondly, irradiance output was validated against DEMROES measurements. Since down-welling shortwave radiation at the surface (SWDOWN) is a grid-averaged output variable, nearest-neighbor interpolation of WRF-CLDDA output was used to co-locate forecasts with the spatially averaged DEMROES observations (red circles, Fig. 2). To compare to the NAM, WRF output was aggregated to

hourly-average irradiance values and spatially averaged over 12 km x 12 km. The primary error metrics used for irradiance forecasts were relative mean bias error (rMBE, Eq. 6), relative mean-absolute error (rMAE, Eq. 7), relative root-mean-square error (rRMSE, Eq. 8), and relative standard error (rSTDERR, Eq. 9):

$$rMBE = \frac{1}{N}\sum_{i=1}^{N}\left(kt_i^* - kt_{m,i}\right), \quad \text{(Eq. 6)}$$

$$rMAE = \frac{1}{N}\sum_{i=1}^{N}\left|kt_i^* - kt_{m,i}\right|, \quad \text{(Eq. 7)}$$

$$rRMSE = \sqrt{\frac{1}{N}\sum_{i=1}^{N}\left(kt_i^* - kt_{m,i}\right)^2}, \quad \text{Eq. 8)}$$

$$rSTDERR = \sqrt{\frac{1}{N}\sum_{i=1}^{N}\left(kt_i^* - kt_{m,i} - rMBE\right)^2}. \quad \text{(Eq. 9)}$$

As opposed to absolute metrics, relative error measures the deviation of

$$kt_m = \frac{GHI_{Observed}}{GHI_{CSK}}, \quad \text{(Eq. 10)}$$

the clear sky index. kt_m (kt^*) is the observed (forecast) irradiance normalized by the expected irradiance given clear conditions. The relative metrics are expressed as a percentage of maximum total irradiance and allow for forecast error to be compared independent of changes in maximum irradiance due to the solar diurnal cycle, geographic position, and time of year. GHI_{CSK} was computed from the Ineichen and Perez (2002) clear sky model which uses the SoDa climatological database for Linke Turbidity (Wald, 2000).

Additionally, error characteristics were spatially quantified using the SolarAnywhere irradiance dataset. Using nearest-neighbor interpolation, SolarAnywhere data was co-located with WRF and NAM grid points. rMAE was then calculated and expressed as a function of time of day. In this way, geographical differences in error could be analyzed.

Lastly, the ability of WRF-CLDDA to accurately quantify daily variability was assessed. Irradiance variability is characterized by ramp magnitude, duration, and frequency of occurrence. Defined as the change in irradiance divided by the time over which it occurs (Δt, Eq. 11), irradiance ramp rates,

$$RR_{\Delta t}(t) = \frac{dGHI}{dt} \approx \frac{GHI\left(t + \frac{\Delta t}{2}\right) - GHI\left(t - \frac{\Delta t}{2}\right)}{\Delta t}, \quad \text{(Eq. 11)}$$

are expressed in W m^{-2} $min.^{-1}$. For each day, ramp rates were calculated for WRF-CLDDA, DEMROES data, and clear sky irradiance for Δt = 5, 10, 30, and 60 min. Daily observed variability statistics were

derived by comparing the cumulative distribution functions (CDFs) of the observed and clear sky ramp rates. On highly variable days, observed ramp rate magnitudes are much larger than the reference clear sky ramp rates (Fig. 5b, inset). Consequently, the observed ramp rate CDF deviates significantly from the clear-sky ramp rate CDF. This difference is quantified using the Kolmogorov-Smirnov Integral (KSI, Beyer *et al.*, 2009) as the integrated difference between the CDFs of observed and clear-sky ramp rates (KSI_{CSK}, Eq. 12):

$$KSI_{CSK} = \int \left(CDF_{Obs.} - CDF_{CSK} \right) dRR \ . \qquad \text{(Eq. 12)}$$

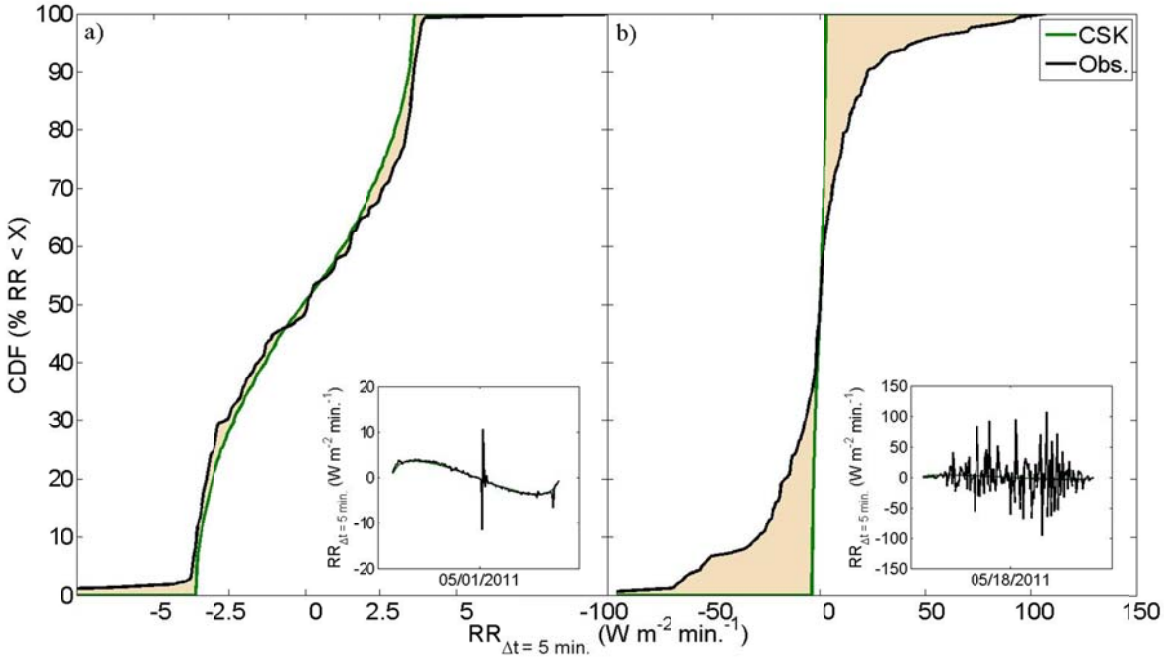

Figure 5: KSI_{CSK} examples for a clear day (5/1/2011, Fig. 5a) and a highly variable day (5/18/2011, Fig. 5b). The main plots compare the CDF of observed (black line) and clear sky (green line) RR with KSI_{CSK} equal to the shaded area. Insets show the instantaneous 5-min. RR.

Fig. 5a depicts a day with little variability. Since the observed irradiance ramp rates match closely with clear-sky ramp rates, the difference between the CDFs and KSI_{CSK} (shaded area) are small. For a highly variable day (Fig. 5b), observed and clear sky ramp rates are significantly different and KSI_{CSK} is large. KSI_{CSK} was calculated for each day and Δt.

At high temporal resolutions it is unlikely that the exact timing of irradiance variability precisely matches observed. Small spatial offsets or phase errors can drastically affect forecast accuracy as measured by MAE or RMSE, even if the predicted cloud field characteristics are correct. Thus, directly comparing forecast to observed ramp rates does not necessarily produce an accurate assessment of model performance. Instead, the variability ratio (V) was used to quantify the accuracy of predicted variability statistics.

$$V = \frac{\sum |RR_{WRF}|}{\sum |RR_{Obs.}|} \quad \text{(Eq. 13)}$$

is defined as the ratio of the sums of forecast and observed ramp rates. The variability ratio estimates if the distribution of forecast ramp rates is under- or over-dispersive. In general, highly variable days are more difficult (and often more important) to predict correctly. To determine how WRF-CLDDA performs as a function of observed variability, V was plotted against KSI_{CSK}. To directly compare V at different time-scales, KSI_{CSK} is multiplied by ramp duration (Δt).

5. Results and Discussion

5.1 Marine Layer Stratocumulus Discussion and Example WRF-CLDDA Forecasts

During May and June of 2011 marine layer stratocumulus clouds are the dominant cloud phenomenon affecting solar irradiance in southern California. Generally, these clouds form when there is sufficient vertical mixing in the presence of a stable atmospheric layer. Typically, temperature decreases with altitude. However, atmospheric layers in which temperature increases with altitude are common for coastal regions of southern California. These layers are stable and suppress vertical motion across their interface. A temperature inversion is created when a high-pressure center over northern California creates strong atmospheric subsidence and drives warm air to sea. As the air descends, it compresses and warms further. Near the surface, the air is significantly cooled by the relatively cold ocean while air aloft remains warm resulting in a temperature inversion. As the synoptic pressure field changes and atmospheric subsidence weakens the altitude of the temperature inversion can increase.

Marine layer clouds form when moist air near the ocean surface is mixed vertically (Pilié *et al.*, 1979) to the temperature inversion. As the air rises, it expands and cools. Consequently, the saturation water vapor mixing ratio (Eq. 3) is reduced and relative humidity approaches 100%. If the temperature inversion is above the level at which water vapor condenses (the lifting condensation level) marine layer clouds will form. Overall, the altitude of the temperature inversion determines the altitude and thickness of the clouds while suppressing vertical mixing with dry, warm air aloft that would dissipate marine layer clouds.

Coinciding with low atmospheric temperatures, marine layer clouds have their greatest spatial extent shortly before sunrise. As the sun rises, temperature and vertical mixing increases, resulting in marine layer cloud cover dissipation. Occurring near the edges of the clouds first, cloud cover evaporation usually occurs at UCSD in the late morning hours. In evening, as low-altitude temperature decreases, marine layer cloud cover may reform.

For 6/13/2011, WRF-CLDDA predicted this general pattern well resulting in an accurate irradiance forecast (Fig. 7). Figure 6 depicts vertical cross sections through UCSD (black line) for the NAM and WRF-CLDDA forecasts. On this day, marine layer clouds capped by the temperature inversion (dashed red line) were predicted by both models. In the NAM, however, the cloud cover retreated to the ocean (≈-117.3°) by 8 PST. WRF-CLDDA predicted thicker clouds that extended inland and persisted until 10 PST and WRF-CLDDA GHI increased significantly. On this day, the dissipation of the marine layer at UCSD was accurately predicted to within 10 min. at UCSD (Fig. 7).

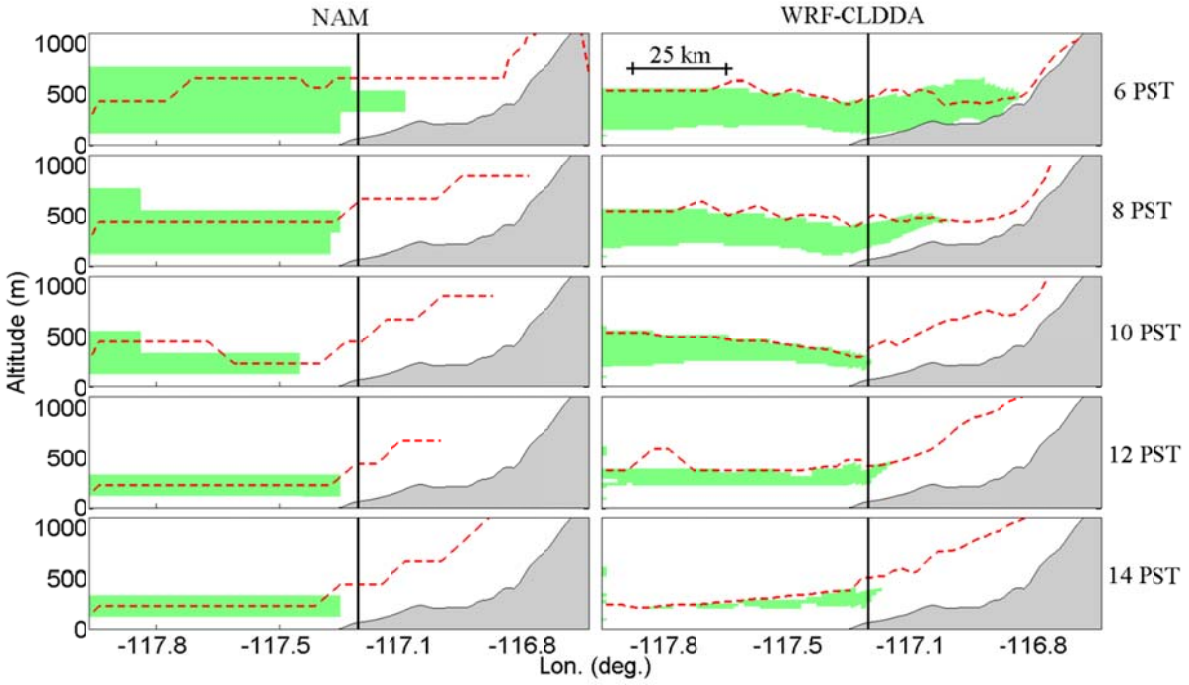

Figure 6: NAM (left) and WRF-CLDDA (right) cross-sections for 6/13/2011 depicting cloud extent (green) and temperature inversion height (dashed red line). The black vertical line marks the location of UCSD. For all forecasts, marine layer cloud cover extent is greatest in the early morning (06 PST). As temperature near the surface increases, the temperature inversion rises and marine layer clouds dissipate (12 PST).

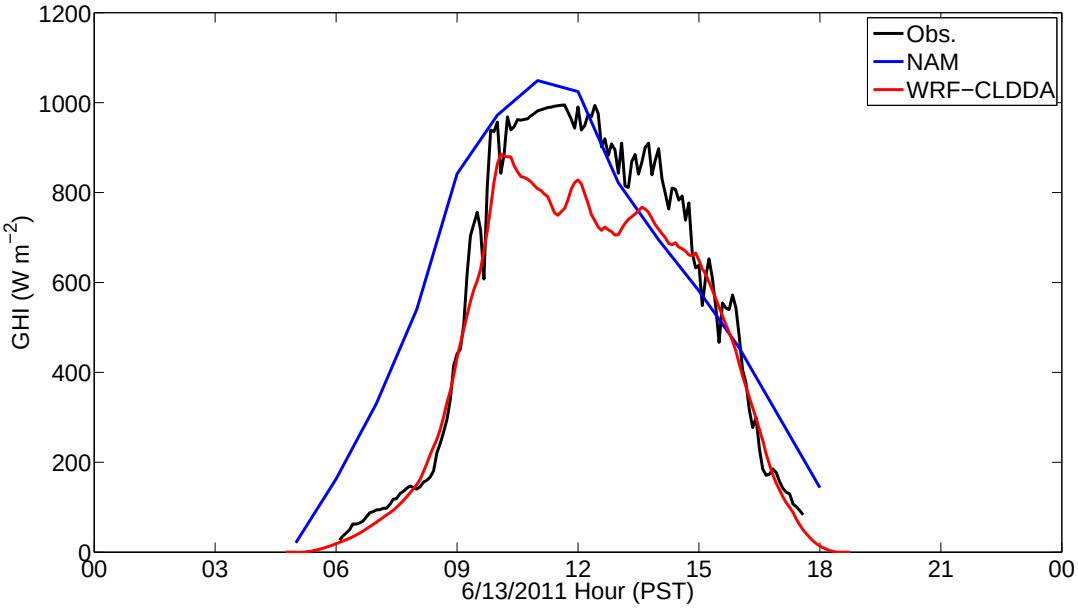

Figure 7: Time-series of 5-min. observed (black), hourly NAM-predicted (blue), and 5-min. WRF-CLDDA-predicted (red line) GHI for 6/13/2011.

5.2 Irradiance Error Metrics

Consistent with marine layer cloud cover, observed clear sky indices (Eq. 10) fit an approximate bi-modal pattern (Fig. 8a) corresponding to clear ($kt_m = 1.0$) and overcast ($kt_m < 0.3$) conditions. Specifically, overcast conditions were common for morning hours (< 09 PST); for over 30% of days marine layer cloud cover resulting in $kt_m < 0.3$ was observed. By 10 PST, clear conditions ($kt_m > 1.0$) were observed most frequently (> 60% of days) and generally persisted until late afternoon (16 PST). In evening (18 PST) overcast conditions were found to return for 25% of days. In principle, kt_m should never exceed 1. Thus, the large frequency of observations with $kt_m > 1$ indicates a shortcoming in GHI_{CSK} (Eq. 10). However, since the clear sky model was similarly applied to observation, NAM, and WRF-CLDDA data, the comparison is valid.

Contrastingly, the NAM (Fig. 8b) intra-day kt^* distribution was dominated by clear conditions ($kt^* > 1.0$) throughout the day. Even for early morning hours, NAM intra-day forecasts rarely predicted overcast conditions, indicating that marine layer cloud cover is routinely under-predicted. For day-ahead forecasts, however, cloudy conditions were more common. For morning hours, the NAM predicted cloudy conditions less frequently (15%) and at a larger kt^* ($kt^* = 0.50$) than observation ($kt_m = 0.25$). Thus, morning cloud cover predicted by the NAM was optically too thin. For mid-day day-ahead forecasts (12-18 PST), the NAM kt^* distribution was inaccurate. Clear conditions were over 20% less common than observed and partially cloudy conditions ($0.50 < kt^* < 0.75$) were 10%-20% more common than observed. As such, the kt^* distribution appears more random than observed.

The WRF-CLDDA intra-day and day-ahead kt^* distributions (Fig. 8), however, matched the bi-modal observation pattern well. The frequency of morning marine layer cloud cover was captured accurately for both intra-day and day-ahead forecasts indicating that WRF-CLDDA correctly predicts the extent and thickness of overnight marine layer reformation.

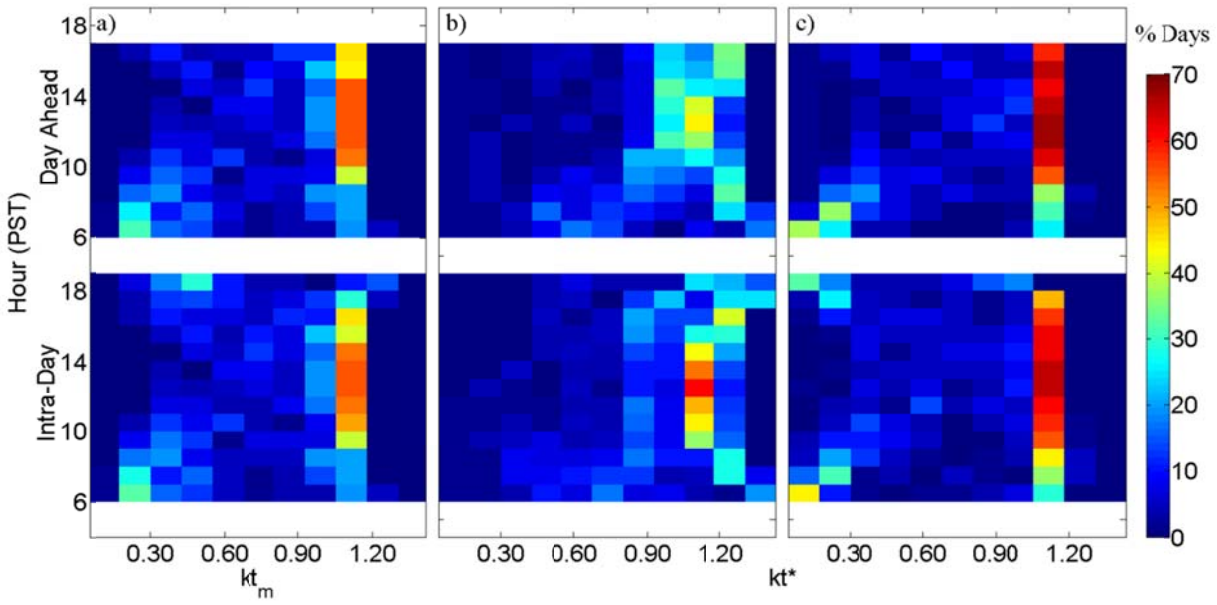

Figure 8: Joint clear sky index (kt_m/kt^*) and time of day (hr PST) histogram for observations (a), NAM (b) and WRF-CLDDA (c) intra-day and day-ahead forecasts for UCSD in May and June 2011.

Table 1: Summary of hourly-average error metrics for persistence, NAM, and WRF-CLDDA irradiance forecasts at UC San Diego. A summary of errors divided by month is provided in Table B1.

	Error	Intra-Day			Day Ahead		
	(% GHI_{CSK})	Pers.	NAM	WRF-CLDDA	Pers.	NAM	WRF-CLDDA
Overall	rMBE	3.3	17.8	0.4	2.7	14.3	1.6
	rMAE	22.4	25.4	21.3	28.3	23.8	18.2
	rRMSE	30.4	33.8	31.1	36.7	32.8	27.5
	rSTDERR	30.2	28.7	31.1	36.6	29.5	27.5

Quantitatively, irradiance error is summarized in Table 1. Here, intra-day (day-ahead) persistence forecasts are calculated by multiplying the hourly-average kt_m from 24 (48) hours prior with clear sky irradiance. As expected, WRF-CLDDA is more accurate than the persistence models; day-ahead rMAE is 11.1% smaller. However, WRF-CLDDA only improves over the 24 hr persistence model by 1.1%. Since the presence of marine layer stratocumulus is dependent on slowly changing, large scale meteorological conditions (e.g. the general circulation pattern and marine temperature inversion characteristics), coastal cloud cover patterns are often similar on consecutive days. Under these conditions, the 24 hr persistence model generally captures the irradiance signal well.

Consistent with previous studies (Mathiesen and Kleissl, 2011), NAM intra-day forecasts are positively biased (rMBE = 17.8%) indicating an under-prediction of coastal cloud cover. Comparatively, WRF-CLDDA irradiance forecasts are only slightly positively biased (rMBE = 0.4%), representing a large improvement in accuracy. Furthermore, improvements are observed in both intra-day rMAE (4.1%) and rRMSE (2.7%). In terms of rSTDERR, however, WRF-CLDDA is 2.3% less accurate. Since relative standard error is the bias-corrected rRMSE it represents the random component of forecast error and can be interpreted as the 'spread' of the forecast error distribution. Thus, though WRF-CLDDA is much less biased, intra-day forecast errors are similarly as random as the NAM.

In general, NWP rMAE and rRMSE increase by 1%-3% between intra-day and day-ahead forecasts (Perez *et al.*, 2011). Here, however, NAM rRMSE decreases by 1% and rMBE decreases by 3.5%. Despite the slight improvement in rRMSE, NAM rSTDERR increases by 0.8% since less of the forecast error can be attributed to systematic bias. This confirms that the day-ahead NAM kt^* is more random (Fig. 8b).

Additionally, WRF-CLDDA day-ahead forecasts are slightly more accurate than intra-day. WRF-CLDDA day-ahead rSTDERR is 27.5% (an improvement of 2% over the NAM). As discussed previously, the day-ahead kt^* distribution indicates that WRF-CLDDA accurately predicts the overnight reformation of marine layer cloud cover. Furthermore, clouds assimilated within the large outer WRF-CLDDA domain likely increase day-ahead accuracy. Since the outer domain of WRF-CLDDA is very large (1500 km x 1500 km), clouds (especially frontal systems) can be assimilated and advected for 24 hours or more before impacting the region of interest and improving the day-ahead irradiance forecast.

Previously, Lara-Fanego *et al.* (2011) found WRF rMBE of 62% - 75% (Table B2) for observed overcast conditions ($kt_m < 0.4$). Overall, it was concluded that WRF predicted clear skies too frequently and that WRF accuracy decreases as observed cloud fraction increases. Here, considering only observed overcast conditions WRF-CLDDA intra-day rMBE was 16.3% (Table B2). While still over-predicting irradiance, this demonstrates that the combination of model configuration and data assimilation increases the

likelihood that cloudy conditions will be forecast correctly. Furthermore, WRF-CLDDA improved most over the NAM for overcast (ΔrRMSE = 10.7%) and cloudy ($0.4 < kt_m < 0.65$, ΔrRMSE = 10.5%) conditions indicating that WRF-CLDDA performs best when clouds are present. Clear conditions ($kt_m > 0.65$) , however, were negatively impacted; NAM rRMSE was 5.3% lower than WRF-CLDDA. Furthermore, Lara-Fanego found rMBE between 2% and 4%, while WRF-CLDDA rMBE was -4.8%. Thus, for some clear observations, clouds incorrectly were assimilated or failed to evaporate in WRF-CLDDA.

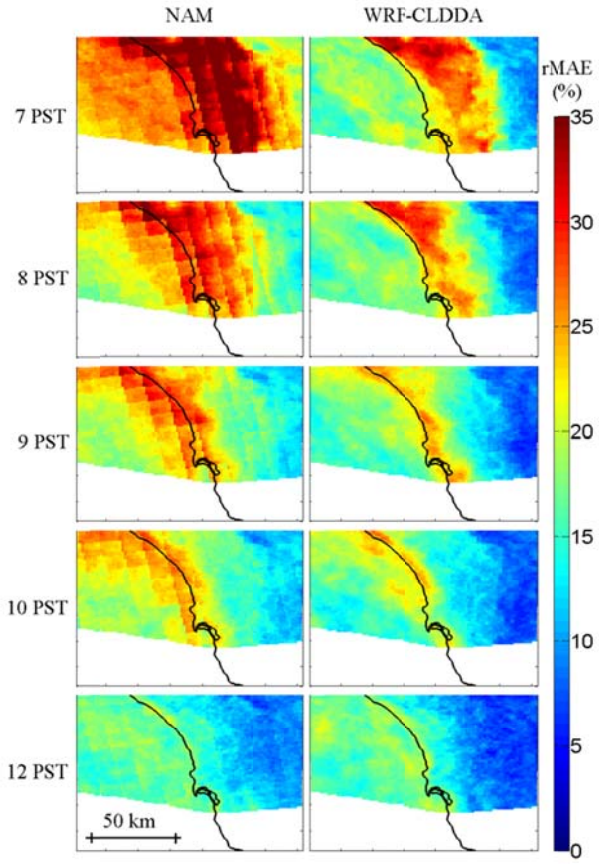

Figure 9: rMAE (% GHI_{CSK}) of NAM (left) and WRF-CLDDA (right) forecasts compared to SolarAnywhere data at several times of day. In early morning hours, NAM forecasts are much less accurate, especially over oceanic and coastal regions, indicating a deficiency in predicting marine layer cloud cover.

Figure 9 shows the spatial rMAE of NAM (left) and WRF-CLDDA (right) irradiance forecasts as a function of time of day. At 7 PST, NAM forecast rMAE is approximately 27% over the ocean. For land areas within 30 km of the coast, rMAE is much higher, exceeding 35% in some regions. Comparatively, oceanic WRF-CLDDA forecasts have rMAE from 17% to 23% and coastal rMAE of 23% to 33%. The improvement over the NAM is largest within 10 km of the coast. These results indicate that for early morning hours, WRF-CLDDA more accurately predicts marine layer cloud cover especially in coastal regions. Later in the day, as marine layer clouds become less frequent, the difference in accuracy decreases. Notably, WRF-CLDDA forecasts greater than 30 km inland are very accurate (rMAE < 5%) regardless of time of day. This is due to infrequent cloud cover in inland regions.

5.3 Variability Analysis

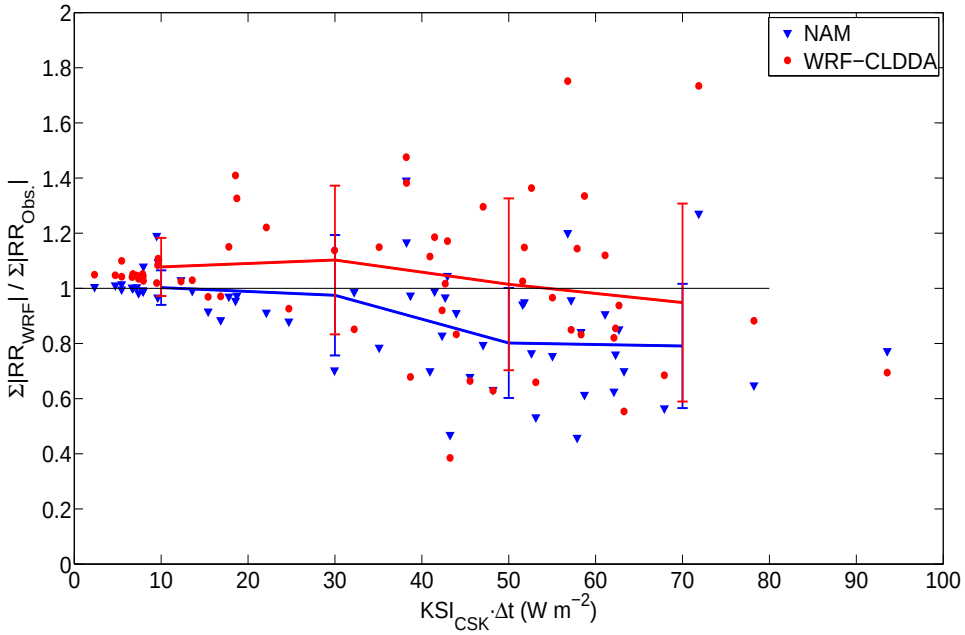

Figure 10: Variability ratio (*V*, Eq. 13, *y*-axis) as a function of the daily variability statistic ($KSI_{CSK}\cdot\Delta t$) for NAM and WRF-CLDDA 60 min. ramp rates. Each dot represents a single day. Lines and bars indicate the mean and standard deviation of *V* in bins of 20 W m^{-2} on the *x*-axis.

Due to its hourly output, the NAM cannot resolve irradiance variability for $\Delta t < 60$ min. Even for hourly ramp rates, though, the NAM is slightly under-dispersive (Fig. 10) with average variability ratios of about 0.9. Only for days with little observed variability ($KSI_{CSK}\cdot\Delta t < 10$ W m^{-2}) does the NAM accurately characterize hourly ramp rates. Additionally, for large KSI_{CSK}, the spread of *V* increases, indicating that for any particular day the variability could be over-predicted by up to 25% or under-predicted by 40%. Since spatial resolution determines the size of resolvable cloud features, this implies that the NAM spatial resolution is too coarse to accurately resolve the cloud features that influence hourly irradiance ramp rates. Essentially, the spatial averaging that occurs over a single grid cell smoothes the variability characteristics of the predicted hourly irradiance time-series. Conversely, the 1.3 km horizontal resolution of WRF-CLDDA is fine enough to capture hourly variability characteristics. However, WRF-CLDDA is more likely to be over-dispersive (predicting too much hourly variability).

At finer time scales ($\Delta t = 5$ min.), however, WRF-CLDDA is consistently under-dispersive, especially for highly variable days (Fig. 11a). For $KSI_{CSK}\cdot\Delta t > 20$ W m^{-2}, WRF-CLDDA predicts less than half of the observed variability for $\Delta t = 5$ min ($V < 0.5$). For $\Delta t = 10$ min., WRF-CLDDA is again under-dispersive (Fig. 11b). However, days for which $KSI_{CSK}\cdot\Delta t < 15$ W m^{-2} are characterized accurately. Only for $\Delta t > 30$ min. (Fig. 11c) does WRF-CLDDA accurately characterize variability for all observed days. Physically, a ramp rate is dependent both on cloud speed and the time over which the ramp occurs. Generally, this can be related to the scale of cloud features that contribute to variability by $\Delta x = U_{Cloud}\cdot\Delta t$. For WRF-CLDDA, $\Delta x = 1.3$ km if clouds are being resolved with sizes on the order of the horizontal discretization. Assuming a typical cloud speed of 12.5 km hr^{-1} implies that WRF-CLDDA should resolve ramp rates with Δt as fine as 6.5 min. However, Fig. 11 suggests that the minimum resolvable Δt is 30 min. As such, using U_{Cloud} = 12.5 km hr^{-1} and $\Delta t = 30$ min., the actual resolved cloud features have a scale of 6.25 km, nearly 5 times larger than the model resolution of 1.3 km. Thus, to resolve irradiance ramp rates accurately at time scales of 5 min., a discretization size smaller than 1.3 km, possibly as small as 250 m, would be required.

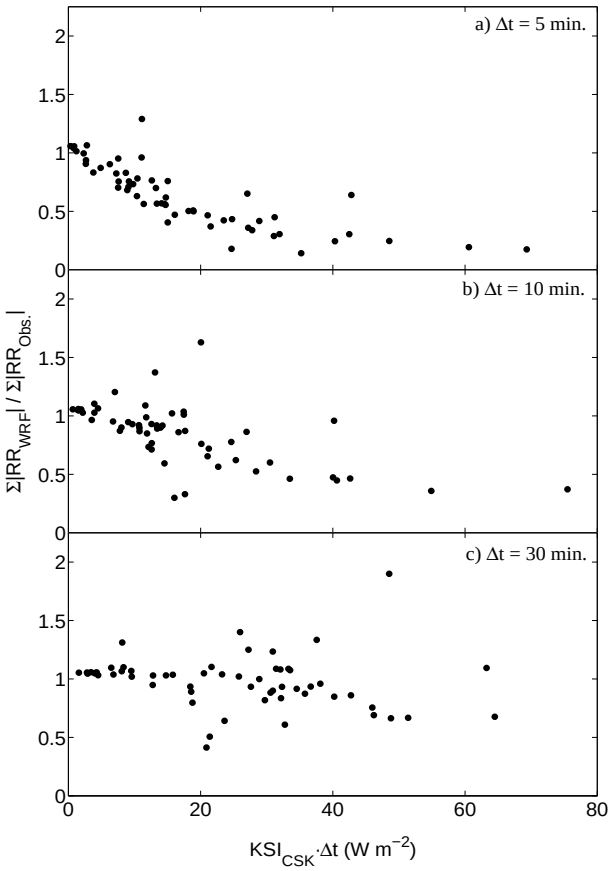

Figure 11: Variability ratio as a function of the daily variability statistic (KSI_{CSK}·Δt) for WRF-CLDDA ramp rates of Δt = 5 min. (a), Δt = 10 min. (b), and Δt = 30 min. (c). Dots represent single days.

6. Summary and Conclusions

Previous studies have shown that most operational NWP models (e.g. the NAM) are inaccurate for solar irradiance forecasting, typically over-predicting GHI and under-predicting cloud cover. Specifically, these errors are exacerbated for summer-time coastal California, when marine layer stratocumulus conditions are common. The source of this error can be traced to three primary sources: Spatial resolution, inaccurate physics parameterizations, and poor model initializations.

To address these sources of error, a high-resolution, cloud-assimilating NWP based on the Weather and Research Forecasting (WRF) model was implemented at the University of California, San Diego for solar irradiance forecasting. Fine horizontal (Δx = 1.3 km) and vertical resolutions were used to promote low-altitude cloud formation. Cloud microphysics, solved by a 2-class scheme in the NAM, was parameterized by the more complex 6-class Thompson model. Additionally, a direct-cloud assimilation system was employed to populate the model initial conditions with cloud cover. To match GOES imagery, clouds were systematically added or subtracted from the model initial conditions by directly modifying the water vapor mixing ratio (q_{vapor}). Using this system, intra-day and day-ahead irradiance

forecasts were created for 5/1/2011 and 6/30/2011 and validated against the dense UCSD pyranometer network.

First, a WRF-CLDDA example forecast was created for a typical marine layer day (6/13/2011). Qualitatively, the WRF-CLDDA simulated cloud field was accurate. In the morning, thick cloud cover penetrated inland nearly 25 km. As the day progressed, cloud dissipation occurred, beginning near the edge of the cloud and progressing westward to the coast. By 12 PST, clouds over land had mostly evaporated and clear skies persisted until evening. In terms of irradiance, this example forecast was very accurate (Fig. 7) and correctly predicted the positive ramp due to cloud cover evaporation to within 10 minutes.

Next, the distribution of forecast clear sky indices was compared against observation. Generally, the distribution of observed clear sky indices fell into a bi-modal pattern (Fig. 8a). Mornings frequently consisted of overcast conditions ($kt_m < 0.3$) while mid-day to evenings were observed as clear ($kt_m \geq 1.0$). For about 25% of days, late-evening overcast conditions were recorded as marine layer cloud cover reformed. Overall, WRF-CLDDA intra-day and day forecasts matched this pattern well (Fig. 8c), indicating that data assimilation correctly populated clouds in the initial conditions and that the model configuration accurately predicted the evening reformation of marine layer cloud cover, even though data assimilation had taken place more than 12 hours prior. NAM forecasts, however, did not match well. In general, the intra-day NAM kt^* distribution was dominated by clear conditions ($kt^* \geq 1.0$, Fig. 8b). Morning overcast conditions were predicted for less than 15% of days indicating that marine layer cloud cover was under-predicted. Cloudy conditions were more common for day-ahead NAM forecasts. Here, however, the kt^* distribution appeared more random, indicating a degradation in forecast skill.

WRF-CLDDA irradiance forecasts were also validated against spatio-temporal averages of six pyranometer measurements. Overall, WRF-CLDDA intra-day forecasts had rMBE of 0.4% compared to 17.8% for the NAM. Furthermore, rMAE was 21.3%, 4.1% smaller than the NAM. rSTDERR, a measure of error randomness, was 2.4% larger than the NAM as a large portion of NAM error was attributed to systematic bias. For day-ahead forecasts (> 24 hours), WRF-CLDDA accuracy did not degrade; rMAE was 18.2% and rSTDERR 27.5%. NAM accuracy, however, deteriorated slightly as rSTDERR increased by 0.8% to 29.5%, confirming that the day-ahead NAM kt^* distribution was more random. In general, NWP rMAE and rRMSE increase by 1%-3% between intra-day and day-ahead forecasts (Perez *et al.*, 2011). Here, however, it was found that NAM and WRF-CLDDA accuracy remained constant. Furthermore, WRF-CLDDA accuracy was established as a function of sky condition (Table B2). The largest improvements over the NAM occurred for overcast (ΔrRMSE = 10.7%) and cloudy (ΔrRMSE = 10.5%) conditions. However, for clear conditions, WRF-CLDDA was less accurate than the NAM (ΔrRMSE = -5.3%) and negatively biased, indicating that for some forecasts clouds were incorrectly assimilated or failed to dissipate in the model. In general, WRF-CLDDA performed best when clouds were observed.

Spatially, NAM and WRF-CLDDA forecasts were validated against SolarAnywhere irradiance data. WRF-CLDDA forecasts were much more accurate than the NAM in the morning (< 9 PST) for oceanic and coastal regions. Especially within 10 km of the coast, WRF-CLDDA rMAE was approximately 10% smaller than the NAM. For later hours (> 10 PST) when marine layer cloud cover was less common, WRF-CLDDA and NAM accuracy was similar. Overall, WRF-CLDDA was demonstrably better when marine stratocumulus conditions were expected. However, when clear conditions occurred, WRF-CLDDA was slightly less accurate than the NAM.

Finally, the ability of WRF-CLDDA and the NAM to characterize irradiance variability was quantified. Using the variability ratio (Eq. 13) and $KSI_{CSK} \cdot \Delta t$ statistic (Eq. 12), the irradiance variability of each day was characterized. For one-hour ramp rates, it was found that the NAM is about 10% under-dispersive for all days, regardless of observed variability. In general, the NAM predicts 1 hr ramp rates with less frequency and smaller magnitude than observed. Likely, this is because of the coarse discretization size of the NAM, where clouds of a small enough scale to affect the irradiance signal on 1 hr are not fully resolved. Conversely, WRF-CLDDA accurately predicted variability at Δt = 60 min. The ability of WRF-CLDDA to characterize variability at finer scales was also evaluated. For ramp rates with Δt < 30 min., WRF-CLDDA was under-dispersive, especially for highly variable days. Based on a typical cloud speed of 12.5 km hr^{-1} and a minimum resolvable ramp rate Δt of 30 min. it was determined that the model-resolved cloud length scale was approximately 6.25 km, nearly 5 times the horizontal discretization size. Thus, in order to accurately resolve ramp rates with Δt = 5 min., a model resolution of much finer than 1.3 km is required. Previous studies, however, have demonstrated that increasing model resolution generally reduces model accuracy (Zack, 2012). As spatial averaging increases, the random component of error is minimized and accuracy improved. The ability to accurately characterize variability, though, will also be diminished.

While high-resolution NWP forecasting with data assimilation was demonstrated for conditions typical of southern California, it is applicable with minor modifications to other regions and meteorological conditions. Changes in the cloud data assimilation procedure may be required, such as in the expected water content (factor 1.1 in Eq. 5) and cloud altitude. For instance, over other regions, the temperature inversion that is characteristic to marine layer stratocumulus clouds is not present. As such, satellite cloud height retrievals must be instead used to place the vertical location of the cloud. Cloud vertical extent can subsequently be derived from the expected cloud type; cumulus clouds can be built between the lifting condensation level and the reported cloud top and cirrus clouds can be assimilated by raising the water vapor content for a thin layer high in the atmosphere. By considering the local meteorology, the method of direct cloud assimilation presented here can be extended to many areas in order to improve solar irradiance forecasting.

7. Acknowledgements

We acknowledge (i) funding by GL-Garrad Hassan, Inc. and the California Energy Commission under contract 500-10-043; (ii) GOES satellite products by the Cooperative Institute of Research for the Atmosphere (CIRA) at Colorado State University under the direction of Matt Rogers and Steve Miller, (iii) Helpful conversations with Stan Benjamin, John Brown, Curtis Alexander and others at the Earth Systems Research Laboratory (NOAA) in Boulder, CO**,** (iv) Patrick Shaw and Daran Rife of GL-Garrad Hassan for assistance and guidance for WRF modeling.

Appendix A. Relationship of Marine Layer Cloud Thickness and Temperature Inversion

Marine stratocumulus cloud location is dependent on the vertical location of the temperature inversion. To quantify this, temperature and relative humidity profiles as measured by 12 UTC Miramar radiosondes were compared for summer months between 2008 and 2011. The location of the temperature inversion was defined as the first atmospheric layer within which the temperature increases with altitude. Cloud location was determined from relative humidity. Atmospheric layers within which relative humidity exceed 95% were considered cloudy. Cloud-top and cloud-base altitude was then calculated and related to inversion height (Fig. A1).

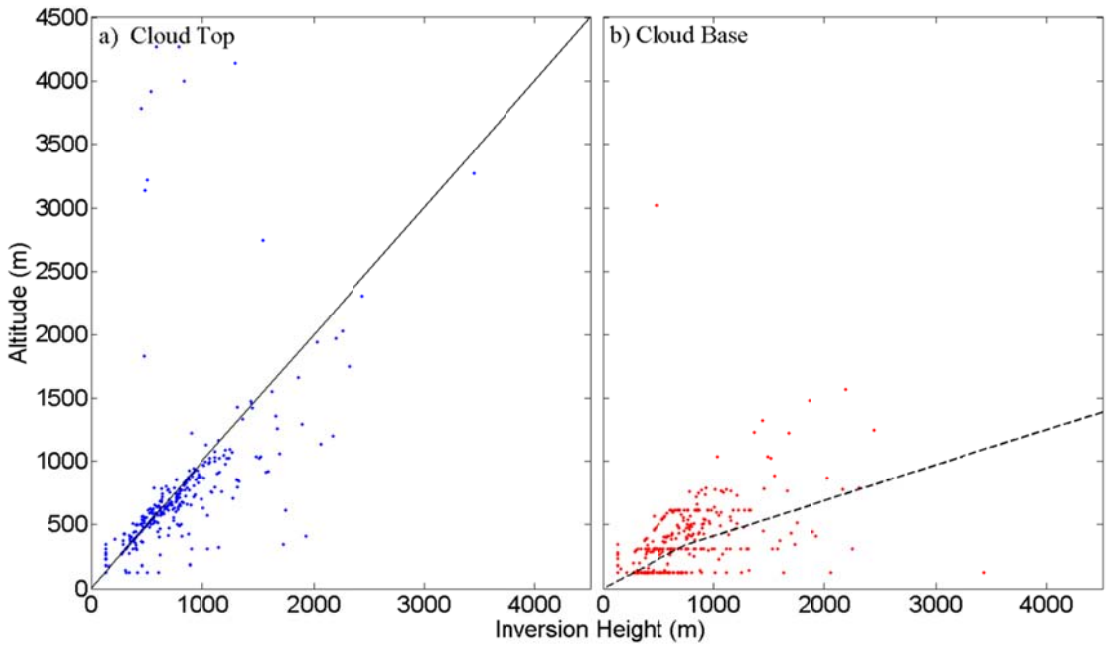

Figure A1: Cloud top (a) and cloud base (b) location as a function of the temperature inversion height. Data was taken from 12 UTC Miramar radiosonde profiles for summer months between 2008 and 2011.

In general, cloud-top location (Fig. A1a) was co-located with the temperature inversion (black line). Though cloud base altitude also increases with the temperature inversion height, it does so at a slower rate (Fig. A1b). Thus, as the inversion height increases so does cloud thickness. The black dashed line in Fig. A1b represents the linear fit to the data as expressed in Equations 1 and 2.

Appendix B. Detailed ΔMAE Tables and Figures

Table B1: Error summary (% GHI_{CSK}) as divided by month.

	Error	Intra-Day			Day Ahead		
	(% GHI_{CSK})	Pers.	NAM	WRF-CLDDA	Pers.	NAM	WRF-CLDDA
May	rMBE	2.0	14.7	-2.8	2.1	13.4	2.2
	rMAE	22.0	22.3	20.4	30.6	24.3	17.5
	rRMSE	31.0	30.0	29.9	39.3	34.6	27.0
	rSTDERR	30.9	26.1	29.8	39.2	31.7	26.9
June	rMBE	4.8	21.1	3.8	3.2	15.0	1.0
	rMAE	22.8	28.7	22.2	27.0	24.0	19.4
	rRMSE	29.7	37.4	32.2	34.8	31.6	28.7
	rSTDERR	29.3	30.8	31.9	34.7	27.8	28.7

Table B2: rMBE and rRMSE error summary (% GHI_{CSK}) as divided by clear sky index. Lara-Fanego *et al.*, 2011 values are reported as the range of annual error between observation sites.

kt_m range	rMBE (%)			rRMSE (%)		
	Lara-Fanego *et al.*, 2011	NAM	WRF-CLDDA	Lara-Fanego *et al.*, 2011	NAM	WRF-CLDDA
$kt_m < 0.4$	[62, 75]	43.1	16.3	[116, 149]	52.0	41.3
$0.4 < kt_m < 0.65$	[13, 20]	34.8	0.9	[35, 45]	47.2	36.7
$kt_m > 0.65$	[2, 4]	6.1	-4.8	[9, 14]	20.0	25.3

8. References

Albers, S., McGinley, J., Birkenheuer, D., and Smart, J., 1996. The local analysis and prediction system (LAPS): Analyses of clouds, precipitation and pressure. *Weather and Forecasting*. **11**(3), 273-287.

Benjamin, S., Kim, D., and Brown, J., 2002. Cloud/hydrometeor initialization in the 20-km RUC using GOES and radar data. *Proceedings of the 10th Conference on Aviation, Range, and Aerospace Meteorology*. American Meteorological Society, Portland, OR, USA.

Benjamin, S., Dévényi, D., Weygandt, S., Brunadge, K., Brown, J., Grell, G., Kim, D., Schwartz, B., Smirnova, T., and Smith, T., 2004a. An hourly assimilation-forecast cycle: The RUC. *Monthly Weather Review*. **132**, 495-518.

Benjamin, S., Weygandt, S., Brown, J., Smith, T., Smirnova, T., Moniger, W., and Schwartz, B., 2004b. Assimilation of METAR cloud and visibility observations in the RUC. *Proceedings of the 11th Conference on Aviation, Range, and Aerospace and the 22nd Conference on Severe Local Storms*. American Meteorological Society, Hyannis, MA, USA.

Beyer, H., Martinez, J., Suri, M., Torres, J., Lorenz, E., Müller, S., Hoyer-Klick, C., and Ineichen, P., 2009. Report on benchmarking of radiation products, Management and Exploitation of Solar Resource Knowledge (MESOR) report contract number 038665, available online at: http://www.mesor.net/deliverables.html. Accessed 3/11/12.

Campbell Scientific, 1996. LI200S Pyranometer instruction manual. Campbell Scientific Technical Specifications, Revision 2/96.

Chow, C.W., Urquhart, B., Lave, M., Dominguez, A., Kleissl, J., Shields, J., and Washom, B., 2011. Intra-hour forecasting with a total sky imager at the UC San Diego solar energy testbed. *Solar Energy*. **85**, 2881-2893.

Dudhia, J., 1989. Numerical study of convection observed during the winter monsoon experiment using a mesoscale two-dimensional model. *Journal of Atmospheric Sciences*. **46**, 3077-3107.

Hu, M., Weygandt, S., Xue, M., and Benjamin, S., 2007. Development and testing of a new cloud analysis package using radar, satellite, and surface cloud observation within GSI for initializing rapid refresh. *Proceedings of the 18th Conference on Numerical Weather Prediction*. American Meteorological Society, Park City, UT, USA.

Hudson, J., and Frisbie, P., 1991. Cloud condensation nuclei near marine stratus. *Journal of Geophysical Research*. **96**(D11), 20797-20808.

Ineichen, P., and Perez, R., 2002. A new airmass independent formulation for the Linke turbidity coefficient. *Solar Energy*. **73**(3), 151-157.

Janjic, Z., 1994. The step-mountain eta coordinate model: Further developments of the convection, viscous sublayer, and turbulence closure schemes. *Monthly Weather Review*. **122**, 927-945.

Janjic, Z., 2000. Comments on "Development and evaluation of a convection scheme for use in climate models." *Journal of Atmospheric Sciencies*. **57**, 3686.

Janjic, Z., Gall, R., and Pyle, M.E., 2010. Scientific documentation for the NMM solver. NCAR Technical Note NCAR/TN 477+STR.

Janjic, Z., Black, T., Pyle, M., Ferrier, B., Chuang, H.Y., Jovic, D., McKee, N., Rozulmalski, R., Michalakes, J., Gill, D., Dudhia, J., Duda, M., Demirtas, M., Nance, L., Slovacek, T., Wolff, J., Bernadet, L., McCaslin, P., Stoelinga, M., 2011. User's guide for the NMM core of the Weather Research and Forecast (WRF) modeling system version 3. 195 pg.

Kain, J., 2004. The Kain-Fritsch convective parameterization: An update. *Journal of Applied Meteorology*. **43**, 170-181.

Lacis, A., and Hansen, J., 1974. A parameterization for the absorption of solar radiation in the Earth's atmosphere. *Journal of Atmospheric Sciences*. **31**(1), 118-133.

Lara-Fanego, V., Ruiz-Aria, J.A., Pozo-Vázquez, D., Santos-Alamillos, F.J., and Tovar-Pescador, J., 2011. Evaluation of the WRF model solar irradiance forecasts in Andalusia (southern Spain). *Solar Energy*. doi:10.1016/j.solener.2011.02.014.

Lin, W., Zhang, M., and Wu, J., 2009. Simulation of low clouds from the CAM and the regional WRF with multiple nested resolutions. *Geophysical Research Letters*. **36**, L08813, doi:10.1029/2008/GL037088.

Lorenz, E., Hurka, J., Heinemann, D., and Beyer, H., 2009. Irradiance forecasting for the power prediction of grid-connected photovoltaic systems. *IEEE Journal of Selected Topics in Applied Earth Observations and Remote Sensing*. **2**(1), 2-10.

Mathiesen, P., and Kleissl, J., 2011. Evaluation of numerical weather prediction for intra-day solar forecasting in the continental United States. *Solar Energy*. **85**(5), 967-977.

Mathiesen, P., Brown, J., and Kleissl, J., 2012. Geostrophic wind dependent probabilistic irradiance forecasts for coastal California. *IEEE Power & Energy Society Transactions on Sustainable Energy*. **99**, 1-9.

Nakanishi, M., and Niino, H., 2006. An improved Mellor-Yamada level-3 model: Its numerical stability and application to a regional prediction of advection fog. *Boundary Layer Meteorology*. **119**, 397-407.

Novakovskaia, E., Sloop, C., and Guo, Z., 2011. The impact of real-time observations on the WRF model surface forecasts. *11th EMS Annual Meeting*, **8**, EMS-2011-605-1.

Otkin, J., and Greenwald, T., 2008. Comparison of WRF model-simulation and MODIS-derived cloud data. *Monthly Weather Review*. **136**, 1957-1970.

Pelland, S., Galanis, G., and Kallos, G., 2011. Solar and photovoltaic forecasting through post-processing of the Global Environmental Multiscale Numerical Weather Prediction Model. *Progress in Photovoltaics: Research and Applications*.

Perez, R., Ineichen, P., Moore, K., Kmiecik, M., Chain, C., George, R., and Vignola, F., 2002. A new operational model for satellite-derived irradiances: Description and validation. *Solar Energy*. **75**(5), 307-317.

Perez, R., Kivalov, S., Schlemmer, J., Hemker, K., Renné, D., and Hoff, T.E. , 2010. Validation of short and medium term operational solar radiation forecasts in the US. *Solar Energy*. **84**(12), 2161-2172.

Perez , R., Beauharnois, M., Hemker, K., Kivalov, S., Lorenz, E., Pelland, S., Schlemmer, J., and Van Knowe, G., 2011. Evaluation of numerical weather prediction solar irradiance forecasts in the US. *Proceedings of Solar 2011, American Solar Energy Society*, Raleigh, NC.

Pilié, R.J., Mack, E.J., Rogers, C.W., Katz, U., and Kocmond, W.C. 1979. The formation of marine fog and the development of fog-stratus systems along the California Coast. *Journal of Applied Meteorology*. **18**, 1275-1286.

Remund, J., Perez, R., and Lorenz, E., 2008. Comparison of solar radiation forecasts for the USA. In: 2008 European PV Conference, Valencia, Spain.

Rogers, E., Black, T., Ferrier, B., Lin, Y., Parrish, D., and DiMega, G., 2001. Changes to the NCEP meso eta analysis and forecat system: Increase in resolution, new cloud microphysics, modified precipitation assimilation, modified 3DVAR analysis. http://www.emc.ncep.noaa.gov/mmb/mmbpll/eta12tpb/. Accessed 3/11/12.

Rogers, E., DiMego, G., Black, T., Ek, M., Ferrier, B., Gayno, G., Janjic, Z., Lin, Y., Pyle, M., Wong, V., and Wu, W.S., 2009. The NCEP North American mesoscale modeling system: Recent changes and future plans. Preprints, *23rd Conference on Weather Analysis and Forecasting* and the *19th Conference on Numerical Weather Prediction*. Omaha, NE. American Meteorological Society, 2A.4.

Sengupta, M., Heidinger, A., and Miller, S., 2010. Validating an operational physical method to compute surface radiation from geostationary satellites. *Proceedings of the SPIE Conference*. San Diego, CA.

Skamarock, W., Klemp, J., Dudhia, J., Gill, D., Barker, D., Duda, M., Huang, X., Wang, W., and Powers, J., 2008. A description of the advanced research WRF – version 3. NCAR Technical Note NCAR/TN 475+STR.

SolarAnywhere, SolarAnywhere Data. Clean Power Research 2012. Available: http://www.SolarAnywhere.com

Thompson, G., Rasmussen, R., and Manning, K., 2004. Explicit forecasts of winter precipitation using an improved bulk microphysics scheme. Part I: Description and sensitivity. *Monthly Weather Review*. **132**, 519-542.

Tselioudis, G., and Jakob, C., 2002. Evaluation of midlatitude cloud properties in a weather and climate model: Dependence on dynamic regime and spatial resolution. *Journal of Geophysical Research*. **107**(D24), 4781, doi:10.1029/2002JD002259.

Xue, M., Wang, D., Gao, J., Brewster, K., and Droegenmeier, K., 2003. The advanced regional prediction system (ARPS), storm-scale numerical weather prediction and data assimilation. *Meteorology and Atmospheric Physics*. **82**, 139-170.

Wald, L., 2000. SoDa: A project for the integration and exploitation of networked solar radiation databases. *Proceedings of the European Geophysical Society Meeting, XXV General Assembly*. Nice, France, 25-29 April, 2000.

Weygant, S., Benjamin, S., Dévényi, D., Brown, J., and Minnis, P., 2006. Cloud and hydrometeor analysis using METAR, radar, and satellite data within the RUC/Rapid-Refresh model. *Proceedings of the 12th Conference on Aviation, Range, and Aerospace*. American Metrological Society, Atlanta, GA, USA.

Wu, W.S., Purser, R.J., and Parrish, D., 2002. Three dimensional variational analysis with spatially inhomogeneous covariances. *Monthly Weather Review*. **130**, 2905-2916.

Zack, J. 2012. Large system variable generation forecasting: Progress and challenges. UVIG Variable Generation Forecasting Workshop. Tucson, AZ. 2/8/2012.